Article:
Hodgkinson, R., Chaffin, S.T., Zimmerman, W.B.J. et al. (2022) Extensional flow affecting shear viscosity: experimental evidence and comparison to models. Journal of Rheology, 66 (4). pp. 793-809. ISSN: 0148-6055

https://doi.org/10.1122/8.0000380

Journal of Rheology

RESEARCH ARTICLE | JULY 01 2022

Extensional flow affecting shear viscosity: Experimental evidence and comparison to models

Richard Hodgkinson ; Stephen T. Chaffin; William B. J. Zimmerman ; Chris Holland ; Jonathan R. Howse

J. Rheol. 66, 793–809 (2022)
https://doi.org/10.1122/8.0000380

πάντα ῥεῖ

Extensional flow affecting shear viscosity: Experimental evidence and comparison to models

Richard Hodgkinson,[1,a)] Stephen T. Chaffin,[2,b)] William B. J. Zimmerman,[1,c)] Chris Holland,[3] and Jonathan R. Howse[1]

[1]*Department of Chemical and Biological Engineering, The University of Sheffield, Sir Robert Hadfield Building, Mappin Street, Sheffield S1 3JD, United Kingdom*
[2]*School of Mathematics and Statistics, The University of Sheffield, Hicks Building, Hounsfield Road, Sheffield S3 7RH, United Kingdom*
[3]*Department of Materials Science and Engineering, The University of Sheffield, Sir Robert Hadfield Building, Mappin Street, Sheffield S1 3JD, United Kingdom*

(Received 30 September 2021; final revision received 10 May 2022; published 28 June 2022)
Published open access through an agreement with JISC Collections 128554

Abstract

The effect of extensional flow on apparent shear viscosity has never previously been *directly* measured nor is it often considered. Here, for the first time, through using a novel flow configuration (two-phase shear response under extensional flow), we have directly measured the effect extensional flow has on the apparent shear viscosity of a viscoelastic polymer solution in a controlled and kinematically mixed manner. We show, via a control transient shear experiment, that the apparent shear viscosity of the solution under mixed deformation depends not only on the shear rate but also on the extension rate and their relative direction: shear thinning being enhanced by parallel and reduced by perpendicular extensional flow, respectively. A 62% reduction in apparent viscosity with parallel extension was seen in this work. We then test the ability of the commonly used Giesekus and Carreau–Yasuda (incorporating generalized shear rate) models to predict the effect of extension rate on apparent shear viscosity against our data. The Giesekus model was found to predict the correct qualitative behavior under both parallel and perpendicular extensional flow, and depending on the fitting parameters, also provided a loosely quantitative agreement. Conversely, the generalized shear rate description does not capture the qualitative behavior, with the most significant errors occurring for perpendicular extension (i.e., expansion) flows. This work emphasizes the rarely noted shortcomings of the latter approach when used for experimental analysis and engineering design when extensional flows are additionally present. https://doi.org/10.1122/8.0000380

I. INTRODUCTION

The shear rheology of a material is perhaps the most prominent and considered factor in understanding flow behavior. Shear rheology is, by definition, studied under a pure shear flow, a process which provides shear viscosity data, η, as a function of the shear rate, $\dot{\gamma}$, typically under steady-state conditions. However, real-world flows may also be kinematically mixed where, along with a shear component, they are also subjected to an extensional deformation. This may be brought about, for example, by channel contractions or expansions. Such flows are incredibly important to industry, the traditional example being polymer extrusion [1–3]—not only for fabrication reasons but also because of the dramatic improvements in mechanical properties it enables [4]. Despite this, we do not yet fully understand these complex flows and the need to do so is as current as ever. This work provides a new insight into shear stress response under mixed flows, and this study is especially pertinent to the following applications:

- Process design for and extensional flow processing of highly anisotropic materials such as graphene fibers (a liquid crystal in solution, cf. discussion later) into next generation high performance materials [5, 6].
- Additive manufacturing (AM) using a extruding nozzle or orifice [7], a process which can leverage the alignment caused by extension [8] but is hampered by a need to better understand the processability of complex materials (especially composites) [7,9] and nuanced requirements on material rheology both during and potentially after deposition/extensional flow (e.g., cements and pastes).
- Application of shear to extensional flow processes for molecular orientation and crystallinity control: rotating mandrels in conventional extrusion [10–13] and controlled application of shear to AM [14,15].
- Systems where extensional flow is generated as a direct consequence of shear coupling from a moving boundary: blade spreading/coating applications [16] and lubricant

[a)]Author to whom correspondence should be addressed; electronic mail: r.hodgkinson@sheffield.ac.uk
[b)]Present address: School of Mathematics and Physical Sciences, University of Hull, Cottingham Road, Hull HU6 7RX, United Kingdom.
[c)]Electronic mail: w.zimmerman@sheffield.ac.uk

flow in bearings [17,18] (lubricants themselves may contain a variety of additives, including polymers).
- Co-extrusion processes where two or more materials are extruded together through a die in a layered structure, recently applied to applications such as fuel cell fabrication [19–21] and lithium-ion battery separators [22,23]. Relative rheological material properties—both shear and extension—are critical to the process and final layer thicknesses, be they polymers [24–27] or ceramics [28–31].

Many other examples exist, and future materials and processing innovations, as well as increasing adoption of computational fluid dynamics, will only make understanding these complex mixed flows ever more critical. Despite this, due to the ubiquity of shear rheology (and perhaps the difficulties of extensional investigations), it may be inadvertently assumed that we can fully characterize the material shear stress response by imposing only shearing flows, i.e., that shear stress σ is only a function of the shear rate $\sigma = f(\dot{\gamma})$, and similarly, $\eta = f(\dot{\gamma})$—or more fully with time dependency, $\sigma = f(\dot{\gamma}(t), t)$[1] and thus, potentially, we may discuss an "apparent" viscosity ($\eta_{app} = f(\dot{\gamma}(t), t)$). Including time dependency is well signposted by the field of oscillatory rheometry, but a more thorough treatment could also include the extension rate ($\dot{\varepsilon}$) such that $\sigma = f(\dot{\gamma}(t), \dot{\varepsilon}(t), t)$ and $\eta_{app} = f(\dot{\gamma}(t), \dot{\varepsilon}(t), t)$—something that cannot be directly measured on a conventional rheometer. In this paper, we explicitly show the fallacy of assuming that the shear response is only $f(\dot{\gamma}(t), t)$.

Throughout this paper, for our results, we will refer to shear stresses or an "apparent" shear viscosity, as distinct from a conventional shear viscosity or shear rheometry, as we will be dealing with nonsteady and kinematically mixed flows. We will also refer to a "transient" shear viscosity (without extension) in difference to our extensional tests, this should also be regarded as "apparent" in nature. For the literature review, "viscosity" is used either due to the source or in a broad meaning of discussing flow resistance.

From theory, assuming that viscosity is a function of the local, instantaneous velocity gradients, the most basic link between extensional flow and shear viscosity (strictly, viscosity, in general) exists in the concept of "generalized shear rate." This parameter replaces the classical shear rate in the generalized Newtonian fluid, or GNF models (the power law and Carreau–Yasuda models being examples), when flows under consideration are not unidirectional. The coupling of extension and shear into one parameter arises from the need to satisfy frame invariance for such flows for which the second invariant of the instantaneous rate of strain tensor is instead used [33]. While under pure shear flows, the generalized shear rate, as defined in Eq. (1) for a 2D flow field, is equal to the classical notion of shear rate, this definition is also sensitive to extension rate. Despite that the generalized Newtonian fluid model "should be used only for shearing flows or at least flows, that are very nearly shearing," it is also often hastily applied to more complex flows ([33], pp. 170–171),

$$\dot{\gamma}_{gr} = \sqrt{2\frac{\partial u}{\partial x}^2 + 2\frac{\partial v}{\partial y}^2 + \left(\frac{\partial u}{\partial y} + \frac{\partial v}{\partial x}\right)^2}. \quad (1)$$

This said, more appropriate relations valid under extension, e.g., the upper-convected Maxwell model under the steady state (and, thus, the Oldroyd-B model equivalently) [34], as well as NEMD modeling for a mixed flow field [35], do also exhibit a dependence: a decrease in shear viscosity when an additional extensional flow is directed parallel to the flow direction, and an increase when directed perpendicularly. We also note that empirical models have been proposed that feature a weighted stress that changes depending on the proportion of shear and extension present, for example, the well-known work of Schunk and Scriven, as summarized by Astarita [36]. While this measure reflects more than just the shear viscosity response to straining, the flow classifier used is not inherently sensitive to the direction (for example, sign) of extension. More recently, Tseng's suggestion [37] as presented is also insensitive to the direction.

Experimentally, we know that extensional flows generates significant alignment and/or extension of anisotropic structures—e.g., unfurling long polymer chains from their Gaussian rest state or aligning rodlike particles. This behavior is paramount to many of the topical examples just given and is evident in a diverse array of x-ray and neutron scattering experiments, covering a wide range of practical situations and materials (reviewed in Bharati *et al.* [38] and exemplified by [39–52]). Corresponding orientation flips are typically observed on transitions from contractions (parallel extension) to expansions (perpendicular extension). We also know that liquid crystals display *directly measurable* anisotropic viscosities when their director is orientated by an external field or surface condition relative to a shear flow, with shear viscosity for nematic liquid crystals aligned across a shearing flow being much greater than when aligned in the flow direction (see Sec. I of the supplementary material for a mini-review and notes) [99]. The viscosity without an imposed alignment lies between these two limits. Thus, it seems reasonable that flow induced alignment and alignment induced viscosity effects may be connected. While liquid crystals are not rheologically directly comparable to polymers under flow, we hypothesize that the orientation, alignment, and extension of polymers under extensional flow may produce qualitatively similar shear stress/apparent shear viscosity effects to nematic liquid crystals with external fields, under both parallel and perpendicular alignment relative to the flow direction.

Here, we experimentally test whether $\eta_{app} = f(\dot{\gamma}(t), \dot{\varepsilon}(t), t)$ [and by virtue, $\sigma = f(\dot{\gamma}(t), \dot{\varepsilon}(t), t)$] by performing apparent shear viscosity measurements simultaneously and *in situ* with the application of controlled, near-constant extension (the following literature examples all contained discrete flow stages). To the authors' knowledge, this is the first time this has been achieved, perhaps as the test is rather nontrivial to perform: extension rates are zero at a solid wall [53], irrespective of the channel shape, or indeed whether this surface is static or

[1]Neglecting other environmental factors such as temperature and pressure. Here, we use the "functional" form of dependences, as highlighted in [32].

propagating along a channel. This rules out conventional methods of measuring shear stress. To achieve this, we use a novel two-phase flow technique, as described in the Experimental Overview section (Sec. II). This technique is then used to investigate a model polymer solution in the Results section (Sec. III). Apparent viscosities measured under extensional flow are compared to those from a transient shear-only control experiment in the Discussion section (Sec. IV). The predictions of some commonly used constitutive models are finally compared against the experimental results in the Modeling section (Sec. V). Conclusions are presented in Sec. VI. The Appendix gives more detail on the methods and the supplementary material [99] contains additional experimental and validation information, among other things.

The only direct measurement of shear viscosity depending on extensional flow that we are aware of in literature was reported by Martin *et al.* [52], where a Couette cell was loaded using a 0.5 mm diameter syringe needle, producing uncontrolled extensional flow. A measurable change in shear rheology compared to a sample previously sheared in the Couette cell was reported. The converse has been more widely studied, where shear is followed by an extensional test [54–60], investigating extensional viscosity, η_E, as a function of shear rate [i.e., $\eta_{E,app} = f(\dot{\gamma}(t), \dot{\varepsilon}(t), t)$]. The limited dependence sometimes seen may be consistent with alignment from the so-called "strong" extensional flow dominating that from "weak" shear flow [61,62]. One may, therefore, expect a stronger dependence when investigating $\eta_{app} = f(\dot{\gamma}(t), \dot{\varepsilon}(t), t)$. We note the outlook of using the technique described here for investigating $\eta_{E,app} = f(\dot{\gamma}(t), \dot{\varepsilon}(t), t)$ in Sec. II of the supplementary material [99].

Liquid crystals gave us directly controllable and measurable evidence that orientation/alignment affects shear viscosity, but few materials can have their orientation imposed directly. Alternative indirect evidence of shear viscosity depending on extension-induced alignment would be variations in velocity profiles (or departures from expected velocity profiles) in channels that produce extensional flow. Specifically, as extension rates vary across the channel width, depending on the velocity profile [53], we expect that a complex nonlinear coupling exists between the velocity profile, extension rates, and, thus, the apparent shear viscosity. For suspensions and composites, flow-fiber orientation coupling with anisotropic viscosities is well known about in both model development and experimental observation [63,64], but there is no reason such a coupling should not be present for systems other than suspensions and, in the case of polymers, probably more dynamic given their elasticity and strain rate dependence. Trebbin and co-workers [51] drew the link between extensional induced alignment and nematic liquid crystals to explain velocity profile variations of cylindrical micelles under extensional flow, with a change to a pluglike velocity profile being observed in their channel expansion region.

Stepping back and considering the broader impact on the field of rheology, the comparison of full field profiles such as velocity (and, e.g., birefringence) data between experiment and modeling represents a substantial body of literature investigations, particularly for complex kinematically mixed flows, alongside which this work certainly aligns (e.g., Lee *et al.* [65]). However, discussions in the literature are often qualitative, and we recommend modest caution be practiced in assigning rather "global" phenomena to specific explanations. For example, in contrast to the previous paragraph, stresses from extensional deformation have also been hypothesized to be the cause of velocity profile changes, certainly with polymers [66]. Furthermore, a recent publication concerning the Oldroyd-B model [67] discusses how transient shear might be affecting flow resistance in a variety of situations—when transient shear is considered in a mixed flow field, it appears the qualitative aspects map to those that could also be expected for shear stresses being a function of the extension rate (noting the extension rate dependence of the Oldroyd-B model), thus masking that two complimentary behaviors might be present. We hope that our work might assist in unpicking the mechanisms involved.

The apparent shear viscosity and velocity profile variations hypothesized in this work would also have noteworthy impacts on two areas of experimental rheology. First, they affect unlubricated extensional experiments, as these rely on the relation that the total channel pressure drop is the sum total of that from shear and extensional effects [2] and on simulation to then subtract the shear contribution (e.g., as performed in the work of James *et al.* [68]). Regrettably, apparent shear viscosity variations would directly impact shear induced pressure drops, and velocity profile variations would change the straining rates (extensional, but also shear) in the flow field from those expected in simulation. In hindsight, this makes pressure drop contribution decoupling, and accurate extensional viscosity measurement, much more challenging. Second, an obvious implication concerns attempts at using geometry profiles (e.g., channel tapers, or to some extent, steps) for in-line shear rheometry, which inadvertently contain extensional flow(s). Not only are the flows of course problematically time-transient, the extensional flow may impact the "shear" rheological data obtained—*even* if shear stresses were directly measured via some suitable method, rather than pressure drops [34].

II. EXPERIMENTAL OVERVIEW

In order to measure shear stress while permitting extensional flow, stratified two-phase flow is adopted. We call this technique "two-phase shear response (under) extensional flow," or ToPSREF.

As shown in Fig. 1(a), an immiscible Newtonian oil flows above and in contact with a non-Newtonian aqueous test phase. Using a suitable technique—here, particle image velocimetry, PIV—the shear rates (defined here as the rate of change of velocity perpendicular to a streamline) immediately adjacent the interface are measured in each phase. As summarized in Fig. 1(d), knowing the shear viscosity of the oil phase permits determination of the shear stress acting on that phase. Assuming this stress is continuous across the interface to the non-Newtonian phase, and knowing the shear rate of this phase, we can thus calculate the non-Newtonian phase's apparent shear viscosity. Imaging is performed at the center of a (symmetric) flow field to constrain shearing to the

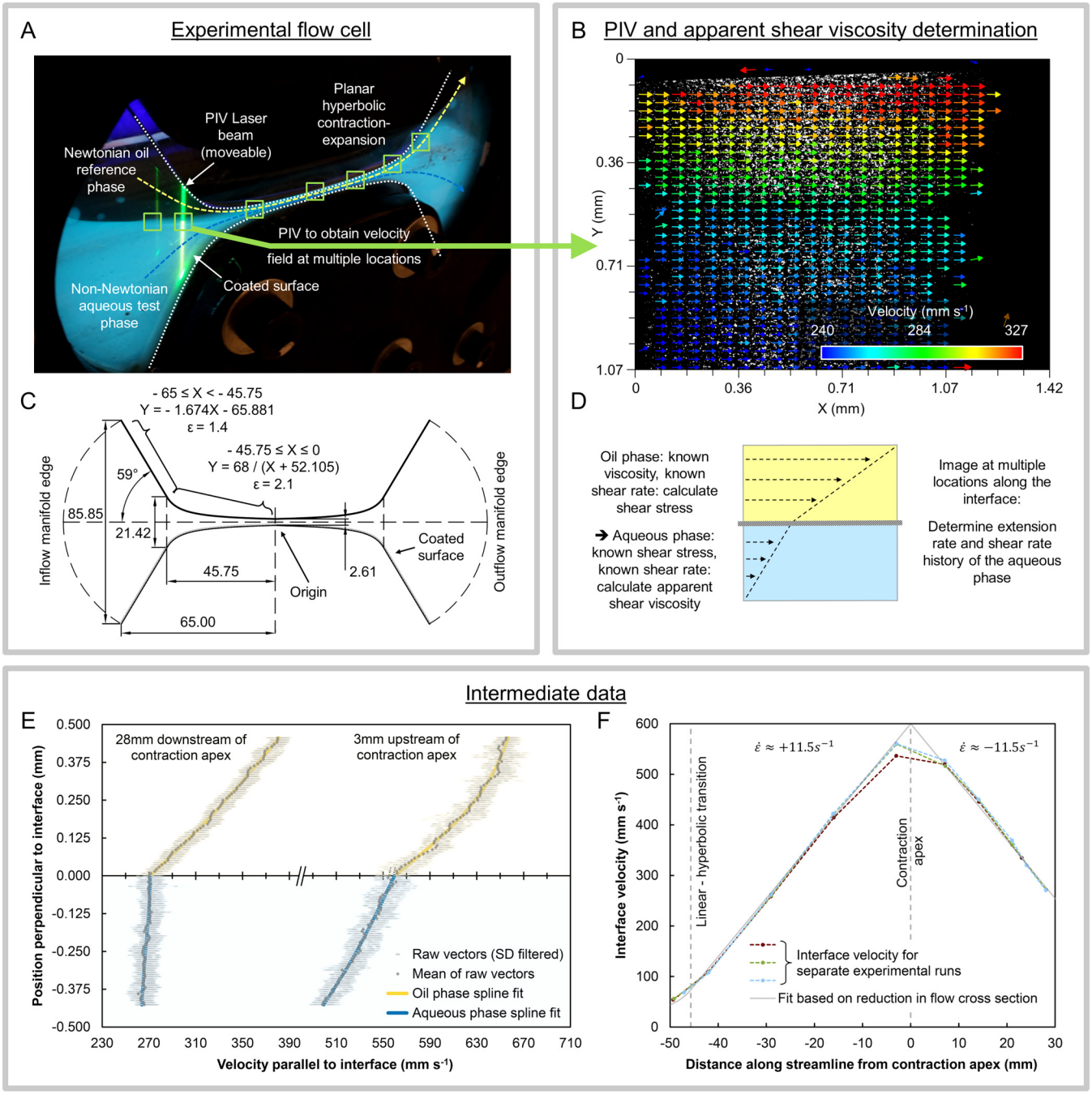

FIG. 1. Concept and implementation of stratified two-phase flow for determining shear stresses and also apparent shear viscosity within an extensional flow field (see color online). In this figure, yellow is used to denote the oil; however, the silicone oil used in this work is actually colorless. Conversely, the otherwise colorless aqueous phase glows blue due to the addition of UV fluorescent dyes. (a) View of the extensional flow channel under flow conditions (dotted white lines mark profiled walls and dashed colored lines mark the fluid flow direction). The fumed silica coated surface is indicated. (b) A typical vector field obtained from PIV cross correlation (discussed in the detailed methods in the Appendix). Vectors for an example experimental run, 29 mm upstream from the contraction apex, are shown overlaid on an image-processed and stacked tracer image (the latter image of the frame pair being shown). Only every 4th vector in X and Y is shown. The two-phase interface is horizontal across the approximate center of the image. (c) Mechanical diagram of the flow channel with salient dimensional details. All dimensions are in millimeters. Distance between front and back walls is 8.4 mm, ϵ denotes the Hencky strain. (d) The conceptual process by which the apparent shear viscosity of the test phase is determined from vector field data such as those shown in (b). (e) Example velocity profiles at either side of the two-phase interface, for an example experimental run, at 3 mm upstream and 28 mm downstream of the contraction apex. Data are processed and fitted as detailed in Sec. IV of the supplementary material [99]. (f) Interface velocities vs distance from the contraction apex. The three experimental runs are shown, together with a fit based on a simple reduction in flow cross-sectional area (gray line). The extension rate corresponding to fit either side of the contraction apex is indicated.

image plane. As the interface may deform, unlike a solid shear stress sensing surface, extensional flow can thus occur at this location. Imaging at several locations down the flow path permits the extension rate to be determined (the rate of change of velocity along a streamline) as well as the shear rate history of a fluid packet.

We note that this is certainly not the first time that two-phase flow with a reference phase has been used to measure

viscosity, albeit via different principles and in simple parallel channels for conventional shear viscosity measurement [69–71]. Furthermore, this work aligns to a large body of literature concerning lubricated extensional experiments (often mutually using hyperbolic or profiled channels) on relatively low viscosity fluids through to polymer melts (e.g., [72–78]). These use lubrication to produce slip in order to mitigate strong velocity profiles and shear pressure drop contributions in attempts to measure extensional viscosity rather than the perhaps "controlled" slip of our reference phase. However, they are subject to much the same challenges (to differing degrees) of the multiphase flow structure and experiment control as present in our setup. PIV is also a commonly used technique, in general, for analyzing extensional flow fields [66,77,79–85]; however, for context, this work differs due to the channel scale chosen and type of illumination. Normally "μPIV" is used with volume illumination for extensional experiments and relies on the lens depth of field (DOF) to select an imaging plane [86]. This work sits between μPIV and conventional PIV scales, making primary use of the lens DOF to select the imaging plane and secondary use of selective illumination to maximize image contrast.

Due to the use of an optical velocity profiling technique and imaging perpendicularly into the cell, it was necessary to match the refractive index of the oil and test phases, otherwise refraction, particularly from the curved interface near the walls, would have made PIV impossible. A planar contraction, with flat sidewalls, was similarly necessary. Alternative configurations to avoid the refractive index matching requirement were considered, including oblique imaging [34], but for PIV measurements, perpendicular imaging proved the only realistic or feasible option. Silicone oil and a solution of poly(ethylene oxide) in a water-glycerol solvent mixture (1.2 wt. % 4×10^6 molecular weight PEO in a 52.88 wt. $\%_{\text{glycerol}}$ glycerol-water mixture) achieved this, albeit functioning here as a very specific model system. Since the interface is now invisible, two fluorescent dyes were added to the aqueous phase to permit experimental control and interface location identification, as well as tracers to both phases for PIV. The moveable optical system used provided a $\sim 1.4 \times 1.1$ mm field of view. Unlike most PIV studies, we are interested in only a small region either side of the interface, and not over the entire width of a channel, even at the smallest extents of the channel [2.61 mm, see Fig. 1(c)]. For concision, the Appendix (detailed methods) gives further information on the PIV setup, solution preparation, and image processing/velocity determination.

A second challenge is in producing the required laterally symmetric flow field, with the lower density oil phase flowing on top of a denser aqueous phase. For any practical small-scale system, however, surface tension dominates over gravity and the oil phase would preferentially contact the channel walls, enveloping a "thread" of the aqueous phase (especially with a Perspex channel). To mitigate this, an air-brushed layer of fumed silica on the lower channel wall, anchored in nail varnish and prewetted with water, served to create a hydrophilic yet oleophobic surface, and is labeled in Figs. 1(a) and 1(c). This pinned the interface location, producing a controlled stratified flow, free from potential instabilities such as capillary breakup. The coating remained stable for at least 6 months even when in contact with the oil phase. The upper and lower channel walls were Perspex for ease of fabrication, but glass sidewalls were used as they appear relatively indifferent to wetting by the separate phases [69,70], though this was more critical to the prior oblique imaging attempts to minimize interface curvature. More information on the surface coating, including demonstration of the coating effectiveness when applied to a Perspex channel, is detailed in Hodgkinson [34]. Selective surface modification requirements lead to a "benchtop," rather than microscale channel common with extensional experiments. Key channel dimensions and parameters are summarized in Fig. 1(c).

A hyperbolic contraction-expansion was used in this work, symmetric about the X and Y axes. The two liquid phases were circulated in separate loops around the experiment by diaphragm pumps with accumulators to remove pulsation. Adjustment of the flow rates of the two phases permitted control over the shear and extension rates probed and optimization of the interface location. Cell outflows were periodically manually adjusted to keep the interface in the middle of the channel expansion region. Filled volume of the whole system was about 1.1 liter of each phase, permitting appreciable relaxation times before a fluid packet was recirculated. Despite a few hours of flow duration and direct phase contacting, total phase cross contamination was on the order of only a few droplets in either direction (mainly, during start-up and visible as drops on the aqueous phase reservoir free surface) and not of rheological concern. The aqueous droplets visible in the oil phase of Fig. 1(a) were attached to the sidewalls and were not moving.

We note that in straight pipe flows, it is possible to use velocity profiles and a single pressure drop measurement to obtain a rheometric flow curve (e.g., ultrasound velocity profile plus pressure drop, UVP-PD [87]), and one may consider alternatively applying this technique to monitor shear stresses or apparent shear viscosity in extensional flows. Aside from issues with hole pressure errors [33] not cancelling, these type of rheometry measurements rely on a specific shear stress distribution across the flow field, which for infinite parallel plates (for example) is linear and of the form $dT_{12}/dy = dP/dx$ [67,88]. However, with extensional flow also present, $dT_{11}/dx + dT_{12}/dy = dP/dx$ and thus the shear stress distribution is unknown and the complex *in situ* measurements developed here initially appear unavoidable. We also note that our experimental measures of shear and extension rates resemble "streamwise" measures in the modeling literature (e.g., Tseng [37]). Some debate currently surrounds this [89,90] [R. Poole, private communication (6 October 2021)]. but it is beyond the scope of this paper to fully discuss it. At the time of writing, we are unsure if a consensus has been or will be reached.

Since our experiment contains a deforming interface, it is important to highlight the potential effects of interfacial rheology on our experiment. Detailed consideration is presented in Sec. III of the supplementary material [99].

III. RESULTS

Before testing the viscoelastic PEO based solution, a Newtonian glycerol-water system was first used to consider the stability of the flow field, develop a shear rate measurement procedure, validate the experiment against an *a priori* known viscosity, and, finally, study the symmetry of the flow field. This process is detailed in the Appendix and Sec. IV of the supplementary material [99]. The measured shear viscosity of the glycerol-water system was 8.76 mPa s for the chosen fitting parameters and the known oil phase viscosity, which compares reasonably with a rheometer measured viscosity in the range of 6.69–7.72 mPa s. Second, as discussed in Sec. IV of the supplementary material [99], inertial stresses as fluid changes velocity through the channel do not appear to impact the shear stress assumptions being made.

Following this, the experiment was drained, cleaned, dried, and reset with the viscoelastic PEO solution as the aqueous phase. Flow rates of 2.25 and 4.27 $cm^3\,s^{-1}$ for the aqueous PEO and silicone oil phases were used, respectively, for producing an interface positioned part way up the edge of a velocity peak in the silicone oil phase. Three experimental repeats (runs) with identical flow conditions were performed, sampling at eight to ten locations along the length of the channel. The same fluid was used throughout all three runs due to the difficulties in resetting the experiment, rather than being replaced with fresh stock solution for each run. Figure 1(e) shows two example velocity profiles from a run at 3 mm upstream and 28 mm downstream of the contraction apex (fitted as described in Sec. IV of the supplementary material) [99]. The change in the test phase apparent shear viscosity is clear. Note the lack of velocity discontinuities or sharp gradients near or across the interface that would be characteristic of interfacial slip or localized viscosity changes (e.g., through polymer depletion). Even if they were present, we only need stress to be continuous across the interface so long as velocity gradient measurements are not affected, and the small exclusion margins applied either side of the interface (see Sec. IV A of the supplementary material) [99] would have assisted in ensuring this.

Figure 1(f) shows the interface velocity at different distances from the contraction apex for all three experimental repeats. In theory, a hyperbolic channel profile should produce constant rates of extension [74], as characterized by the velocity gradient. Here, however, aqueous phase rheology and variations in the associated interface position would be expected to cause departures from this. In fact, extension rates in Fig. 1(f) are very nearly constant. The gray line shows a best fit based on a reduction in the flow cross-sectional area, giving extension rates of about $+11.5\,s^{-1}$ in the contraction and $-11.5\,s^{-1}$ in the expansion regions. Velocities are also identical from run to run, despite the experimental runs being performed on different days, giving confidence in the flow setup repeatability. Total Hencky strain in the constant extension rate region based on the geometry [2.104, Fig. 1(c)] is almost equal to that based on the velocity increase fit [2.096, Fig. 1(f)], which, similarly, is surprising. An extension rate of $11.5\,s^{-1}$ corresponds to a change in velocity across an imaging region of about $16\,mm\,s^{-1}$, which, in addition to experimental scatter, explains the spread of (here, standard deviation filtered) raw vector velocity values in Fig. 1(e).

Considering the extension rates achieved, the Weissenberg number (here defined for extension rates, $Wi = \tau\dot{\epsilon}$) must be greater than 0.5 for significant accumulation of macromolecular strain [66]. Oscillatory rheology at 1% strain on the test solution was limited in accuracy but showed a crossover in storage and loss moduli at 7.6 Hz (n = 6, SD = 2.6 Hz) showing the fluid relaxation timescale to be about 0.13 s. Time temperature superposition was attempted but showed deviations from the linear data shifts required. Based on this value $Wi = 1.5$ for this experiment, satisfying the criteria for significant macromolecular strain.

Figure 3 shows the apparent shear viscosities of the test solution as determined by this experiment with the presence of extensional flow. Viscoelastic systems, however, exhibit time dependent rheology (for example, stress overshoot in flow start-up [90]), and a control experiment is now required with the same shear rates—and same shear history—as in the extensional experiment, but without extensional flow. To achieve this, the data in Fig. 1(f) permitted the aqueous phase shear rate data to be translated into the time domain and programed, via fitting to exponentials, into a conventional rheometer (see the detailed methods in the Appendix). Recreating the exponential shear rate histories is especially important as exponential shear is considered, like extension, to be a "strong" flow [91].

Figure 2 shows the time—shear rate data from the extensional experiment (gray points), programed profile (gray dotted line), and the shear rates as achieved by the rheometer (black line) for an example experimental run. The contraction apex corresponds to 120.5 s. The tests were performed based on the separate shear rate data from each of the three repeats of the extensional flow experiment, each using an aqueous phase fluid sample extracted at the end of the corresponding experimental run. Despite minimal cross contamination, care was taken to avoid the free surface while extracting these samples from the associated circulating fluid reservoir of the experiment. Samples were also gravitationally separated (manner akin to a separating funnel) between storage and loading into the rheometer to further avoid introducing any oil films into the measurement geometry, and the geometry cleaned with acetone between each test.

To consider the effects of upstream flow history, these tests incorporated an estimate of the upstream pipework shear rates in the two different pipe diameters used and the advection timescale through the entry region of the flow cell. These are also shown in Fig. 2. Pipe flow lasts from 0 until 108 s and is calculated based on the average shear rate and residence time across all fluid packets, with both parameters being weighted by a fluid packet's contribution to the overall flow rate. After this, from basic analytical considerations of the flow cell geometry and assuming that once in the flow cell a fluid packet remains on the cell centerline, an advection time of 12.5 s until the contraction apex was estimated, most of which has near zero shear rate. Additionally, these transient tests were repeated on a 400 s estimate of the timescale for a fluid packet to circulate around the flow loop. The

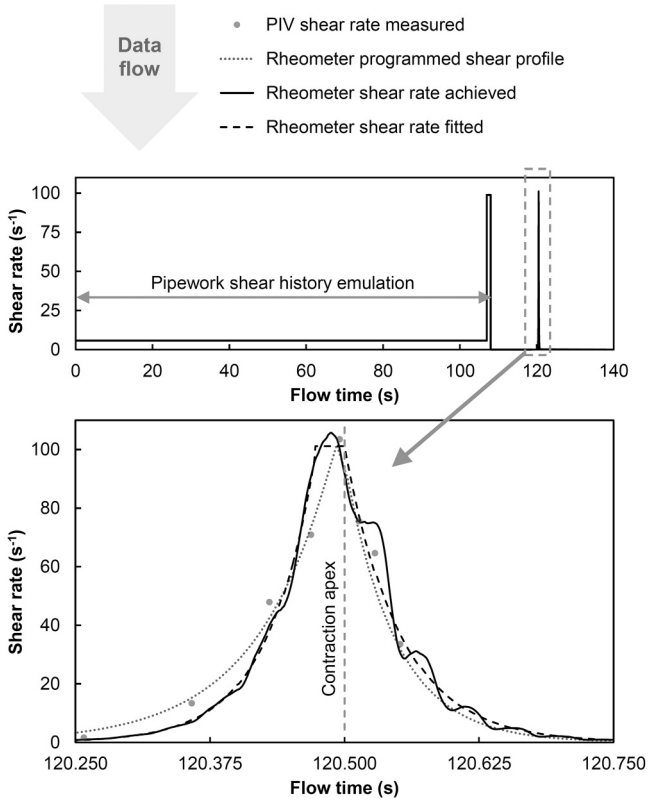

FIG. 2. Example data of a transient shear control experiment for an experimental run. The upper plot shows the shear history profile used to emulate the passage of a fluid packet through upstream pipework and the hyperbolic flow geometry, the lower plot highlights the flow geometry. In the lower plot, the shear rates from the extensional experiment (gray points) and the programmed shear profile fitted through them (gray dotted line) are shown, together with the shear rates subsequently achieved in the transient shear experiment by the rheometer (black solid line) and, finally, fitted (black dashed line) for calculating the "transient" viscosity.

upstream pipe flow and flow loop circulation history did not produce a discernible impact on the results. This is expected as the 12.5 s advection time before a fluid packet reaches the contraction apex is much longer than the solution relaxation time previously measured (0.13 s). Conversely, the advection timescale through the contraction-expansion region (0.5 s in Fig. 2) gives a Deborah number of 0.26 relative to the relaxation time of the solution. This suggests history effects are modestly important for these transient measurements.

The rheometer shear rate oscillations visible in Fig. 2—particularly after 120.5 s—are due to the rheometer motor control and could not be improved further with the damping options available, though the shear stress data were much more continuous. Using this raw data directly produces an oscillating value for the fluid "transient" shear viscosity. To address this, the shear rates achieved by the rheometer were then subsequently fitted to a rising exponential, flat region, and falling exponential, as shown with the black dashed profile, before calculating the "transient" viscosity. This treatment is justified in Sec IV. Due to accumulation of slight time offset errors during the prior pipe flow steps of the rheometer program (typically occurring 0.1 s later than desired), manual time registration of the extensional experiment and rheometer data was necessary. A compromise was sought between placing the rheometer shear rate peak at or close to the contraction apex and best representing the lower shear rates in the regions upstream and downstream of the apex. It would be expected, but not necessarily the case, that the shear rate peak occurred at the contraction apex. This compromise results in the peak in the fitted shear rate data occurring slightly before the channel apex in Fig. 2, and, likely, the similar observable offsets in Figs. 3 and 5.

Unlike in the extensional flow experiment, polymer depletion could be an issue in these transient experiments if it manifested as a wall slip. If wall slip did occur, this would serve to reduce the shear stress or viscosity recorded, which would only reinforce any evidence of parallel extension reducing apparent shear viscosity. This said, Kang *et al.* [92] looked for wall slip with a 2 wt.% 4×10^6 molecular weight poly(ethylene oxide) aqueous solution via comparing viscosity data from 366 to 150 μm gap acrylic microchannels and found "no significant difference" between them, and thus "no distinguishable slip velocity." They also present data from a mechanical rheometer with Couette tool sets (material not stated), which similarly shows no difference to the microchannel data, thus covering a wide span of gaps from a 150 μm gap channel where slip effects would be the most severe (and reasonably appropriate to our 0.5° rheometer geometry used) up to comparatively large gaps.

IV. DISCUSSION

So far, we have been generally concerned with comparing the apparent viscosity in the extensional and transient shear cases; however, we may also compare shear stress directly for two reasons.

First, apparent viscosity somewhat mitigates for differences in shear rate profiles between the two experiments, as visible in Fig. 2, whereas comparing shear stress assumes perfect shear rate recreation. A viscosity basis thus initially appears preferable. Here, however, we are dealing with a transient viscosity, and such terms require careful use (Petrie [93] underlines this in the context of extensional rheology). Focusing on the transient shear experiments, transient viscosity only considers the instantaneous shear rate and is meaningful only if shear stresses also changed instantaneously (or, the system is memory-less). However, the more that stress depends on memory effects, e.g., with the viscoelastic system being studied here, the less valid this concept becomes. The system tends to smooth out shear stress variations against time (e.g., compare the stresses in Fig. 5 later to the shear rates in Fig. 2) and sudden rate changes due to rheometer motor control thus severely influence this transient viscosity value. To alleviate this, the shear rate fitting detailed previously provides an inherently smooth representation of the shear rate to determine viscosity from without issues of defining some form of moving average or fluid specific memory function. It also tracks the raw shear rate data well, in part, as the rheometer was programed with exponential functions initially. However, this treatment will also cause its own degree of error, and, thus, neither a stress nor apparent viscosity comparison basis is perfect.

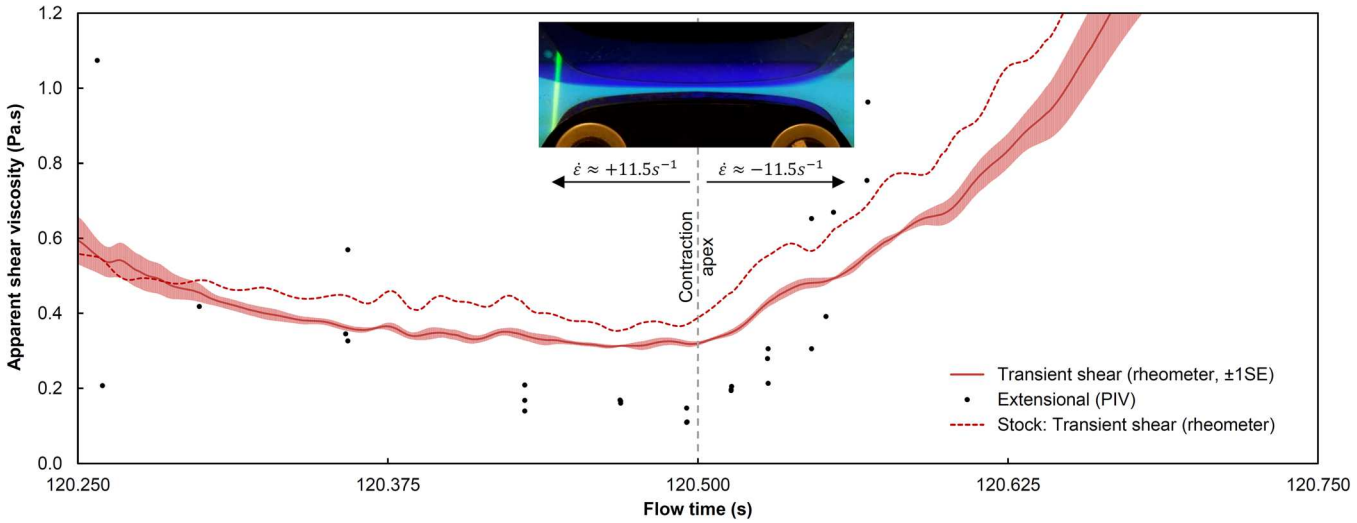

FIG. 3. Comparison of aggregated data from the three extensional flow experiments (black points) and their associated transient shear experiments (solid line with shading to ±1 standard error) on an apparent shear viscosity basis. A transient shear experiment on the stock solution is also plotted (dashed line). The inset photo is illustrative and does not map to the X axis in any manner except highlighting the apex location. A shear stress basis is presented in Fig. S5 of the supplementary material [99].

Second, in the extensional experiment, a characteristic level of velocity scatter means that the determination of low shear rates, with shallow gradients, is subject to a large degree of error. This occurs for the aqueous phase at locations far upstream and downstream of the channel apex [e.g., see Fig. 1(e) at 28 mm downstream]. At these locations, a pair of velocity derivatives are being used to determine the aqueous phase apparent shear viscosity and thus viscosity values vary significantly, while errors in stress measurements, based solely on the higher oil phase shear rates, remain modest (if strictly, it only tends to hide the fact that the shear rates fitted to program the rheometer in this region were equivalently scattered). The shear stress representation thus provides a more stable representation of this data, but for different reasons compared to the transient shear case. Fortunately, however, the apparent shear viscosity data are least scattered at the location of most interest—the channel apex.

Given this discussion, we herein present data in both apparent shear viscosity and shear stress depictions.

Data from the extensional and the respective control (transient shear) experiments are now combined in Fig. 3 (apparent shear viscosity basis) and Fig. S5 of the supplementary material (shear stress basis) [99]. As previously, 120.5 s corresponds to the location of the channel apex. The "stock" curves are detailed shortly. The runs are aggregated in Fig. 3 for presentation purposes and presented separately in Fig. S5 [99]. For a comparison against the steady-state viscosities or stresses associated with the shear rates experienced by the fluid, rather than transient values, consult the Carreau–Yasuda results in the Modeling section.

First, we consider the experiments in isolation. There is a definite spread of apparent shear viscosity values in the extensional experiment data for the reasons stated, the scatter giving an indication of measurement uncertainty and reproducibility. In both the extensional and transient shear experiments, we see a shear thinning style behavior as expected for our test solution and as evidenced in Fig. 4. The transient shear experiment runs vary between each other since they are using independently fitted rheometer profiles and separately recovered fluid samples, aside from basic experimental variability. The dashed line shows a transient test using stock solution (i.e., never contacted with oil in the extensional experiment) and using the shear rates from "run 1" of the extensional experiment. Between this and the three samples extracted from the extensional flow experiment, there is a slight apparent viscosity difference throughout the experiment (reproducible), which may be attributable to solution degradation as discussed in Sec. VI of the supplementary material [99]. Beyond this, however, there is no obvious systematic trend in viscosity between the shear experiment and extensional experiment runs—see Fig. S5 [99]—which would be indicative of the formation of an optically invisible

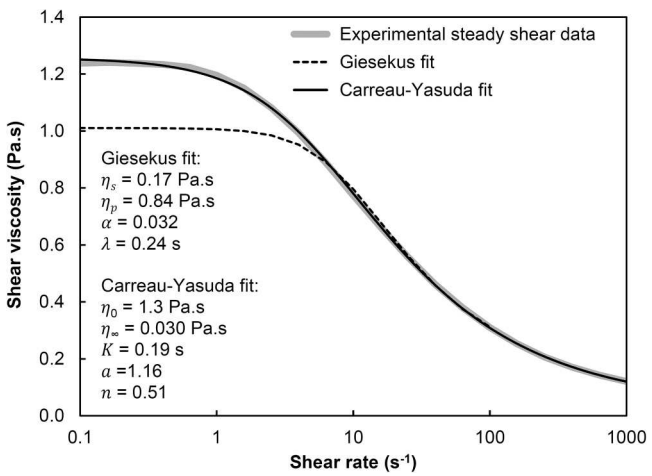

FIG. 4. Experimental steady shear viscosity data for the PEO solution tested (stock solution) and fits to this data for the Giesekus and Carreau–Yasuda models. See the text for details regarding differences between how these fits were conducted/weighted.

(and particularly, in the case of the transient experiments, time-stable) two-phase emulsion.

Comparing the extensional and transient shear cases in Fig. 3, much before 120.375 s, the viscosity values are too scattered for comments on the effects of extensional flow. Shear stresses are slightly above the control experiments in Fig. S5 of the supplementary material [99] but so are the shear rates (e.g., compare with Fig. 2). Beyond this point, however, we can see a definite trend of apparent shear viscosity in the presence of extensional flow directed parallel to the velocity direction dropping below that for the transient shear experiments. Average viscosity under extensional flow reaches a minimum at the measurement location before the contraction apex of 122 vs 319 mPa s for the transient shear experiments—a 62% reduction and well beyond the level of experimental errors seen in the verification experiment. Stresses fall similarly, with a 54% reduction. Section IV A of the supplementary material [99] explores variations in the curve fitting process [as originally presented in Fig. 1(e)] to show that this key result is not an artefact of arbitrary parameter choice.

As we pass 120.5 s, we move into the expansion region of the channel with extension directed perpendicular to the velocity (and shearing) direction. Elastic stresses will have become accumulated by this point and likely play a role. Tolerating the scatter in the extensional flow case, we see a trend of apparent shear viscosities climbing faster than and surpassing those in the transient shear case as would be expected for polymer chains now being aligned across the shear field. Shear stresses in Fig. S5 [99] give a similar picture; while a crossover is not present with the data obtained, a coarse extrapolation suggests that one would occur. In this region, the rate of apparent viscosity increase is being driven not just by chain relaxation but by perpendicular extensional flow; perhaps via augmenting an extended chain—Gaussian coil—orthogonally extended chain transition or by revolving a pre-extended chain. Either way, a crossover time comparable to or shorter than the relaxation timescale measured by oscillatory shear rheometry previously (7.6 Hz or 0.13 s) might be expected: here about 0.05 and 0.08 s after the apex for the shear viscosity and shear stress case, respectively (summarized in Table I). These crossover delays are, of course, tentative as they are additionally sensitive to the time registration previously described between the extensional and transient shear experiment datasets.

In the extensional experiments, data points were not collected beyond 50 mm upstream and 28 mm downstream of the contraction apex. The former is due to distortions from the inlet manifold presence; the latter due to slow drift of the interface position via outflow imbalances and the presence of the aqueous phase swell as visible in Fig. 1(a). With more data points upstream, extension rates would be lower, and we would expect to see a convergence of data from the extensional and transient shear experiments. With more data points downstream, the same would be expected after a continued increase in apparent shear viscosity under perpendicular extensional flow.

TABLE I. Summary and comparison of experimental and modeling "crossover" times between shear and shear with extension data, together with relaxation times or associated parameter values.

Data	Figure	Plot crossover time relative to 120.5 s (s)	Relaxation time (s)
Experimental—stress	S5	~0.08	~0.13 (osc rheo)
Experimental—viscosity	3	~0.05	~0.13 (osc rheo)
Giesekus—transient shear fitted—stress	5(a)	0.043	0.092 (fitted λ)
Giesekus—transient shear fitted—viscosity	S6(a)	0.044	0.092 (fitted λ)
Giesekus—steady shear fitted—stress	5(b)	0.114	0.24 (fitted λ)
Giesekus—steady shear fitted—viscosity	S6(b)	0.115	0.24 (fitted λ)

V. MODELING

To substantiate the implications of this work, we now test the predictions of the Giesekus and Carreau–Yasuda models against the experimental data just obtained. This is intended as an exemplar study given the single experimental system and condition set studied in our experimental work.

First, the Giesekus model [94] is defined in Eqs. (2)–(5). We chose this model as it is a commonly used model in the literature and is applicable to systems beyond the dilute limit [95,96] (including being applied to high molecular weight concentrated PEO solutions previously [96]). The Giesekus model is also capable of capturing both elastic and shear-thinning behaviors vs other more simple viscoelastic models such as Oldroyd-B and, certainly, avoids known shortcomings of the Oldroyd-B model in extensional flows in particular [33]. This said, the Giesekus model is also *by no means* the only model that could be considered for comparison and is used similarly as an example case here—addressing the wide range of models available in the literature is beyond the scope of this paper. We found that a single modal Giesekus model, in general, failed to fit our data in the processes herein described, however, the introduction of a solvent viscosity dramatically improved the quality of the fit. We have thus incorporated the viscoelastic effects through an extra-stress tensor,

$$\boldsymbol{\sigma} = -P\boldsymbol{I} + 2\eta_s\boldsymbol{D} + \boldsymbol{\tau}, \tag{2}$$

$$\boldsymbol{\tau} + \frac{\alpha\lambda}{\eta_p}\boldsymbol{\tau}^2 + \lambda\overset{\Delta}{\boldsymbol{\tau}} = 2\eta_{1p}\boldsymbol{D}, \tag{3}$$

$$\overset{\Delta}{\boldsymbol{\tau}} = (\boldsymbol{v}.\nabla)\,\boldsymbol{\tau} - (\nabla\boldsymbol{v}\,\boldsymbol{\tau} + \boldsymbol{\tau}\nabla\boldsymbol{v}^T), \tag{4}$$

$$\boldsymbol{D} = \frac{1}{2}(\nabla\boldsymbol{v} + \nabla\boldsymbol{v}^T). \tag{5}$$

The value $\boldsymbol{\sigma}$ is the total stress comprising of a Newtonian component and $\boldsymbol{\tau}$ is the extra-stress tensor, which arises due to non-Newtonian effects. The parameters η_s and η_p are the

solvent and polymer viscosity, respectively; λ is the relaxation time; and α is the anisotropy parameter. $\boldsymbol{v}$ denotes the velocity field, P denotes the pressure, $\boldsymbol{D}$ is the rate of strain tensor [defined by Eq. (5)], $\nabla \boldsymbol{v}$ is the velocity gradient tensor, $\boldsymbol{I}$ is the identity tensor, and $\overset{\Delta}{\boldsymbol{\tau}}$ is the upper-convected Maxwell derivative defined by Eq. (4).

The velocity field, $\boldsymbol{v}$, required to solve Eq. (2) is conventionally obtained via the Navier–Stokes equations where the system involves solving a series of nonlinear partial differential equations. However, if we impose a velocity field, then Eq. (2) can be solved along each streamline using the method of characteristics, which removes the complex two-way coupling of the velocity field and extra-stress tensor (however, this may not conserve momentum). As we have the shear rate and extension rate as function of "travel time" (in either the extensional or transient shear experiments), we use a Lagrangian description, which simplifies Eq. (4) into three ordinary differential Eqs. (6)–(8),

$$\frac{d\tau_{11}}{dt} = -\lambda^{-1}\left(\tau_{11} + \frac{\alpha\lambda}{\eta_p}\left(\tau_{11}^2 + \tau_{12}^2\right) - 2\eta_p\dot{\varepsilon}\right) + 2\dot{\varepsilon}\tau_{11} + 2\dot{\gamma}\tau_{12}, \tag{6}$$

$$\frac{d\tau_{12}}{dt} = -\lambda^{-1}\left(\tau_{12} + \frac{\alpha\lambda}{\eta_p}\tau_{12}(\tau_{11} + \tau_{22}) - \eta_p\dot{\gamma}\right) + \dot{\gamma}\tau_{22}, \tag{7}$$

$$\frac{d\tau_{22}}{dt} = -\lambda^{-1}\left(\tau_{22} + \frac{\alpha\lambda}{\eta_p}\left(\tau_{12}^2 + \tau_{22}^2\right) + 2\eta_p\dot{\varepsilon}\right) - 2\dot{\varepsilon}\tau_{22}. \tag{8}$$

We integrate these equations in MATLAB using the stiff solver ode15 s. Since experimentally our upstream advection timescale, 12.5 s, was much longer than the fluid relaxation time measured, the specified initial conditions for our model will likely have a negligible effect. We thus assume Newtonian behavior (i.e., $\boldsymbol{\tau} = 2\eta_p\boldsymbol{D}$) as an initial stress condition *a priori* and check this assumption shortly.

In order to obtain the Giesekus model constants—η_s, η_p, α, and λ—we use the ODE solver to map the predicted shear stress σ_{12} from the model onto experimentally measured shear stress for a particular situation. For this we have two independent datasets, we can map to the transient shear stress from the control transient shear experiments and the steady-state shear stress from a steady shear solution characterization. For simplicity and to avoid complex and subjective weighting choices, we do not attempt to simultaneously fit to multiple datasets in this work (which could additionally include normal stress data, as well as either of the shear stress datasets) and instead present both our steady and transient shear fitted cases separately, allowing us to consider two different yet justified sets of model parameter values. We used the constrained Nelder–Mead amoeba algorithm to minimize, via a least-squares approach, the difference between the predicted shear stress and the experimental shear stress. Conventionally, in rheometer software, model parameters are fitted via viscosity data—if we used this basis for fitting to our transient viscosity data specifically, the fit may be weighted by values away from our key transient dynamics where transient viscosity values are the lowest and additionally rely on data where asymptotically low shear rates are attempting to be imposed by the rheometer. By using shear stress, the fits are dominated by data around the contraction apex region (which is also superficially the location of most interest), if at the expense of not capturing zero shear behavior accurately. The fits can be seen for the steady shear case in Fig. 4 (dashed black line fitted to thick gray line) and for run 1 of the transient shear case in Fig. 5(a) (gray line fitted to black line). The low shear rate viscosity deviations of the steady shear parameter fit are evident—in part due to these deviations, we chose to only fit the model using shear rate data from 0.1 to 100 s^{-1}, the range of shear rates experienced in the extensional experiments. Zero shear viscosity deviations are similarly evident in the transient fitted parameters by considering the zero shear viscosity ($\eta_s + \eta_p$). In our fitting, we did not attempt to enforce a solvent viscosity (η_s) as sometimes conducted in the literature [96]. This was to permit maximum flexibility in the model to accommodate our unusual transient source data and shear stress basis (high shear rate weighting). We note that both the fitted solvent viscosities for the Giesekus model (and the following η_∞ Carreau–Yasuda parameter) are significantly higher than the viscosity of the glycerol-water solvent used (around 6.6 mPa s); however, physically PEO is less soluble in glycerol than water and competition for hydrogen bonding may have altered the effective solvent composition [97]. The Nelder–Mead algorithm requires an initial estimate for the parameters, we used the steady shear parameters as a guess. The transient shear fitting was performed using shear rate against time data before shear rate fitting described in Sec. III was applied, viz., transient viscosity issues discussed previously. For this approach, since we in fact have three transient experiment "runs" with two repeats per transient experiment, we may report average model parameters, assuming that the fluid is independent between runs (e.g., no progressive cross contamination or degradation effects). This gives values of 0.19 Pa s, 0.42 Pa s, 0.084, and 0.088 s for η_s, η_p, α, and λ, with standard deviations of 0.024 Pa s, 0.040 Pa s, 0.022, and 0.014 s, respectively, for transient fitted. For the steady shear fitting, we obtained values of 0.17 Pa s, 0.84 Pa s, 0.032, and 0.24 s, respectively. With regard to λ values, since our fitted relaxation time is indeed $\ll$12.5 s, our Newtonian initial condition choice is justified. We also see, as summarized in Table I, that relaxation times from the two fitting routes are in the same order of magnitude as our oscillatory rheometry value (and given the discussion in Sec. IV, initially note both are also longer than the time taken for experimental viscosity values to "cross over" in the channel expansion region). In general, with regard to model fitting, a full parameter space survey was not conducted, and we found multiple solutions that appeared to give similarly reasonable appearance fits to the experimental data. As a result, we cautiously consider these fitted values potentially somewhat empirical in nature, but adequate for superficially exploring what behaviors the Giesekus model might be capable of capturing.

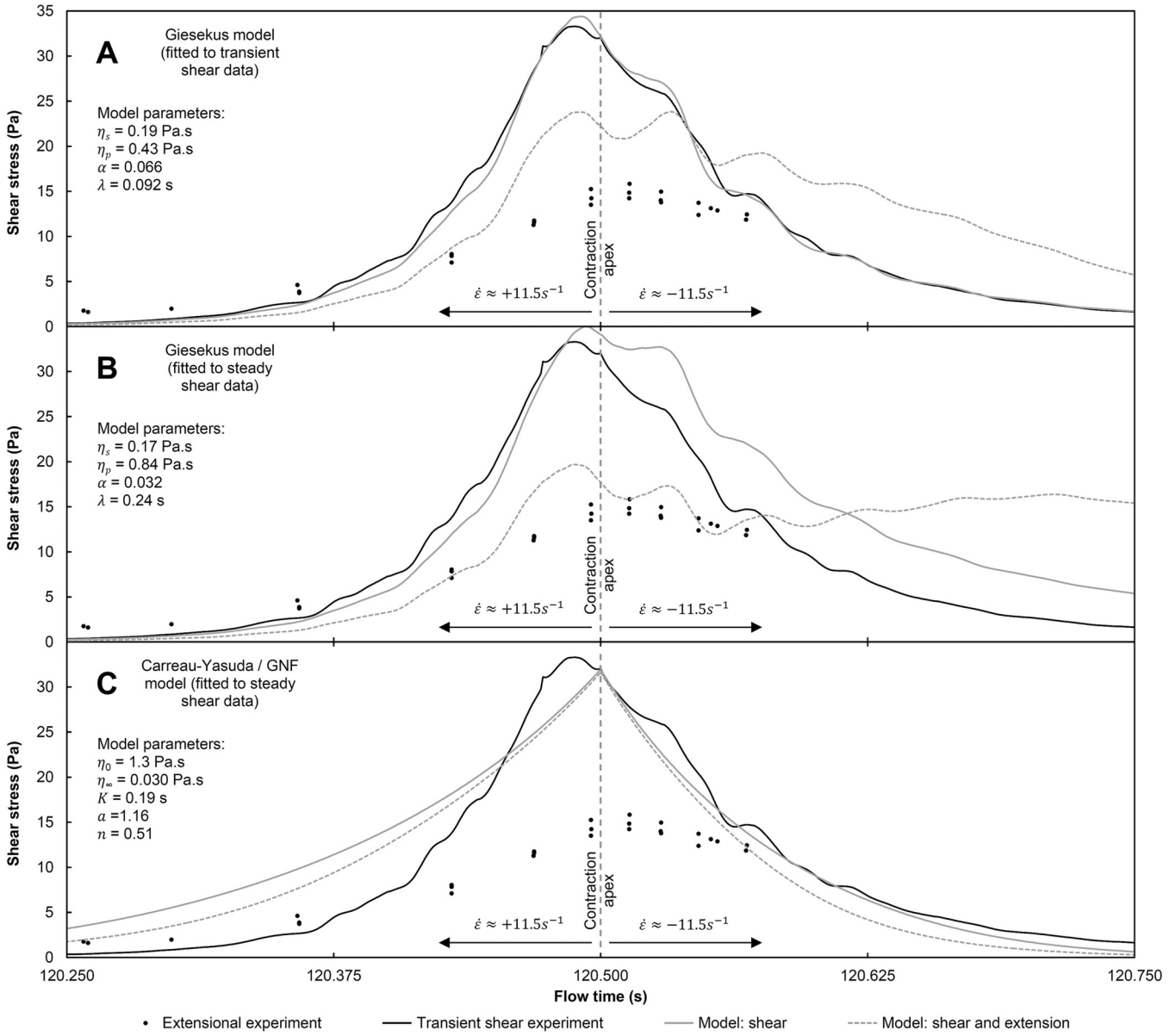

FIG. 5. Comparison of the extensional experiment shear stress data (black points) for all runs and transient shear experiment data (black line) for an example run to model predictions with and without extension for the Giesekus [panes (a) and (b)] and the Carreau–Yasuda model [pane (c)]. As described in the text, the solid gray line is fitted to the solid black line in pane (a) to obtain the model parameters, while fitting for parameters in panes (b) and (c) is conducted in Fig. 4. Apparent shear viscosity plots are presented in Fig. S6 of the supplementary material [99].

In order to highlight the comments about the generalized Newtonian fluid/generalized shear rate description made earlier in Sec. I, the simpler empirical Carreau–Yasuda model is now defined in Eq. (9). This model is chosen again as it is commonly used in engineering. We incorporate the generalized shear rate definition given earlier in Eq. (1) and apply values of $(\partial u/\partial x)^2 = (\partial v/\partial y)^2 = \dot{\varepsilon}^2$, $\partial u/\partial y = \dot{\gamma}$, and $\partial v/\partial x = 0$. This would also be performed with other empirical models, e.g., power law, and the results here for Carreau–Yasuda under extension are thus equally pertinent. Model parameters were obtained from a standard rheometric shear sweep on the stock solution and curve fitted in the rheometer TRIOS software (which we understand uses a least-squares viscosity basis), giving values of $\eta_0 = 1.26$ Pa s, $\eta_\infty = 0.0296$ Pa s, $K = 0.194$ s, $a = 1.16$, and $n = 0.505$. The fit is also presented in Fig. 4 (black line to thick gray line). For this model, since we are concerned with comparing the models to the experimental extensional data rather than between themselves, we evaluate the exponential shear rate profile previously fitted through extensional experiment data (i.e., as subsequently programed into the rheometer in the process outlined in Fig. 2) rather than what the rheometer achieved for an experimental run under consideration,

$$\frac{\eta - \eta_\infty}{\eta_0 - \eta_\infty} = [1 + (K\dot{\gamma})^a]^{\frac{n-1}{a}}. \tag{9}$$

Figure 5 now compares the model predictions of shear stress with experimental data, with apparent shear viscosity instead being presented in Fig. S6 of the supplementary

material [99]. For clarity, we focus on data from one example experimental run (and use the Giesekus model with least-squares fitting parameters obtained for that run) rather than averaging data across experiments—the other experimental runs produce similar conclusions. All models are shown with shear only and shear with $\pm 11.5\ s^{-1}$ of extension. Aggregated extensional experiment data points for all three runs are, however, shown to aid trend identification.

From Figs. 5(a) and 5(b) or S6(a) and S6(b) [99], we can immediately see that the Giesekus model predicts qualitatively the correct response (apparent shear viscosity or shear stress decrease and increase) with the application of extensional flow. With regard to the location of the crossovers present in pane (a) or (b), as summarized in Table I, they fall at times loosely comparable to and either side of the crossovers in the experimental stress or apparent viscosity data and in both cases, they occur at timescales less than their relaxation time parameters (as equivalently discussed in the case of the experimental relaxation time in Sec. IV). For the transient fitted case in pane (a), the model with shear only fits the transient shear experimental data well, as intended. With shear and extension, the shear stress (or apparent viscosity) falls by about half of that seen in the experimental data. Conversely, for the steady shear fitted case in pane (b), the predicted stresses under transient shear do not agree as well as previously, but it is surprising to see the stresses before and the stress peak at the contraction apex align well with the experimental data, if not the predictions after the contraction apex. The most surprising outcome is that with shear and extension, the predicted shear stress or apparent viscosity values then fall close to the extensional experiment data attained. We cautiously feel that this may be just a fortuitous result of the parameter fitting process in our case, however. Despite this, between the two sets of fitted parameters used and despite their subjective nature, these results do show that the Giesekus model is, on the whole, capable of capturing the degree of apparent shear viscosity dependence on extensional flow seen in the experimental work conducted.

In the case of the Carreau–Yasuda model for shear, we note that, interestingly, shear viscosities in the experimental transient shear case reach those of the model (i.e., steady shear); though, due to the complexity of transient behavior, we refrain from calling this a "limiting value" of viscosity. The model also shows a surprising amount of correlation after the apex, at least perhaps helped by the polymer chain-pre-extension at the preceding higher shear rates. However, conversely, in the channel contraction region, the viscosity or stress values do not coincide (thus, underlining the importance of comparing the extensional experiment data to a transient shear control experiment and not steady shear). With regard to the effects of extension, evidently, we see that the generalized shear rate description is qualitatively incorrect, exhibiting only a shear stress (or viscosity) reduction on application of extension, regardless of the applied direction. Furthermore, the numerical dominance of high shear rates in this relation causes the effects of the numerically modest extension rate to become extremely small at the contraction apex, in general contrast to the behavior seen in the experiment. This underlines the statement in the Introduction that the generalized shear rate description should only be used for essentially shearing flows, and, once again, we advocate caution against inadvertently applying it to more complex scenarios. This is certainly the case for test systems similar to our polymer solution in perpendicular extension (expansion) flows.

VI. CONCLUSIONS

Flows of complex fluids subjected to mixed deformations are important in an array of circumstances, yet little is known about their rheological response under such conditions.

In this work, we gathered supporting literature suggesting that extensional straining may affect the apparent shear viscosity of a complex fluid when under a kinematically mixed flow. An experiment (ToPSREF) was designed capable of testing this hypothesis, consisting of a mixed flow experiment containing both shear and extension in a controlled manner, and a control experiment with the same shear history, but no extension. This experiment was verified with a Newtonian system before being used to test a model poly(ethylene) oxide solution in a glycerol-water solvent.

It was found for this viscoelastic model system that extensional flow in a contraction (i.e., directed parallel to the shearing direction) caused a substantial apparent shear viscosity reduction (62% for the conditions studied here) compared to that under pure shearing flow with the same time-transient shear rate history. Extensional flow in a subsequent expansion (i.e., directed perpendicular to the shearing direction) caused the apparent shear viscosity to then rise faster than, and eventually surpass, that under pure shearing flow. This agrees with how such a system might be hypothesized to behave from literature evidence.

The predictions of the Giesekus constitutive model and those of the generalized Newtonian fluid/generalized shear rate definition (here, the Carreau–Yasuda model) were then contrasted to this experimental data. While the determination of the Giesekus model parameters by fitting is unavoidably subjective, we found that the Giesekus model has the ability to qualitatively and near quantitatively capture the directional dependence of extensional flow to changes in apparent shear viscosity for the experimental conditions used and extent of data points captured. The time point at which apparent viscosity in the extensional case surpasses that in the transient shear case on exiting a contraction-expansion channel was also found to be loosely comparable. The generalized shear rate definition/Carreau–Yasuda model, on the other hand, does not show any directional dependence on the extension rate or qualitative agreement to the experimental data and is especially erroneous in the context of expansion flows. We reiterate statements in the literature [33] that great caution should be exercised when applying such relations to complex engineering flows.

This work studied one test system at one set of experimental conditions as a proof of concept—the authors hope that this work will be built on in the future to study a wider range of materials, solution compositions, and flow conditions (particularly, Deborah number range) critical to testing

existing and developing new fluid models. While this work hypothesized that molecular orientation/flow alignment plays a crucial role in the apparent shear viscosity variations measured under extensional flow, no *in situ* molecular orientation measurements were conducted: something that future integration of additional experimental techniques could provide a tantalizing insight into.

ACKNOWLEDGMENTS

This work was indirectly supported by the European Union's Horizon 2020 research and innovation programme under Grant Agreement No. 713475, which enabled the purchase of the DHR2 rheometer used. EPSRC Grant Nos. EP/K005693/1 and EP/I019790/1 funded the RA post occupied during the rheometer use and supported a PIV system upgrade, respectively. We are also grateful to TA Instruments (Europe) for the loan of the 0.5° 60 mm diameter cone and plate geometry used and Dow Chemical Company (Europe)/Chempoint for the kind donation of various grades of Polyox (including the WSR-301 used here). The lead author was funded under a University of Sheffield Ph.D. scholarship. The sponsors had no direct involvement in the work described. Commercial goods and equipment are identified herein to fully describe the experiment—this does not represent an endorsement of a particular product or supplier. R.H. would also like to thank the Chemical and Biological Engineering department's workshop staff for many impromptu discussions and Michael Beeston, of Oxford Lasers, for PIV training. Thank you also to Professor David Harbottle (University of Leeds) for comments on our supplementary material interfacial rheology discussion and Christina Stimson (University of Sheffield) for proofreading our manuscript.

AUTHOR DECLARATIONS

Conflict of Interest

The authors declare that they have no known competing financial interests or personal relationships that could have appeared to influence the work reported in this paper.

Author Contributions

R.H. conceived, built, performed, and analyzed the results of the experiments. S.T.C. conducted the constitutive modelling described and analyzed the predictions of the models against the experimental results. S.T.C. also offered much encouragement with this work both over the course of and after the respective Ph.D.s (personal thank you from R.H. to S.T.C.). R.H. and S.T.C. wrote the manuscript. W.B.J.Z. and J.R.H. supervised the Ph.D. projects. C.H. offered input to data analysis and the use of the DHR2 rheometer for rheological measurements as well as loan of the Abbe refractometer. All authors reviewed the manuscript.

DATA AVAILABILITY

The raw and processed PIV data required to reproduce the findings of this study are openly available to download from the repository indicated under [98]. The data organization is detailed in the appendix of Hodgkinson [34]. Both the Newtonian and viscoelastic data are presented. The transient shear data are available on reasonable request to the corresponding authors at this time.

APPENDIX: DETAILED METHODS

As previously described, the two liquid phases used for the main work consisted of a silicone oil and a PEO water-glycerol test solution, carefully matched in refractive index. Due to this as well as rheological considerations, the experiment was carried out in a temperature-controlled room with fully enclosed flow system to mitigate evaporation. K type thermocouples on the inlet and outlet of each phase gave an average fluid temperature for all experiments of 22.7 ± 0.5 °C.

The silicone oil used (Allcosil 200/50 from J. Allcock & Sons Ltd, UK) has a Newtonian viscosity of 50.0 mPa s to within ±2% at 22.7 °C and over a shear rate range of 0.5 to 500 s^{-1}. This was measured on a TA Instruments DHR2 rheometer with a concentric cylinder geometry (larger viscosity variations occurring at lower shear rates, possibly due to instrument sensitivity). Note that off-the-shelf vehicle lubricants *should not* be used for these experiments, on account of possible polymeric additives (viscosity index modifiers, alluded to in Sec. I) and also surfactants, which could create issues with interfacial rheology (see Sec. III of the supplementary material) [99]. As for the PEO solution, 1.6 l of 1.2 wt. % 4×10^6 molecular weight PEO (Dow Chemical Company Polyox WSR-301) in a very close initial estimate of glycerol-water solvent composition for the refractive index requirement was prepared by stirring at 60 °C for 4 days in an airlocked container until fully dissolved and free of visible particulates. Fine-tuning of the refractive index was then performed via small amounts of water/glycerol addition (<8 cm^3) giving a final resulting composition of ∼1.2 wt. % 4×10^6 molecular weight PEO in a 52.88 wt. $\%_{glycerol}$ glycerol-water mixture. A glycerol-water (53.55 wt. $\%_{glycerol}$) solution served as a Newtonian fluid to validate the experiment. The Newtonian solution viscosity (22.7 °C, concentric cylinder geometry) reproducibly varied from 6.69 mPa s at 2.5 s^{-1} (lowest practical stress) gradually increasing to 7.72 mPa s at 500 s^{-1}, though this is a low viscosity to be measuring in a mechanical rheometer. The nominal viscosity of the PEO glycerol-water solution used is elaborated in Sec. VI of the supplementary material [99]. Refractive index matching of these solutions was performed with an Abbe refractometer operated at the PIV imaging wavelength of 532 nm and the same ambient temperature of the flow experiment. The accuracy of the refractive index matches attained and their effect on spatial accuracy was tested with the Newtonian system: the effect of sweeping the fluid interface across a reference grid viewed through the camera system with a deliberate small, known refractive index mismatch (larger than that typically achieved) was almost imperceptible, showing only a 5–10 pixel movement. Note also that for the viscoelastic system, flow birefringence would have caused an index shift but this was estimated to be much smaller than that associated with the errors of the matching procedure. During preparation of the aqueous solution silver

coated glass tracer particles were added for PIV velocity imaging and two dyes for fluid phase visualization: Potters Industries LLC (USA) SG02S40 (nominal size 2–10 μm, at 0.16 g l^{-1}), "Ebest Rhodamine B" from FastColours LLP, UK (at 2.5 mg l^{-1}), and "Bestoil Pyranine 01" from FastColours LLP, UK (at 30 mg l^{-1}), respectively. The former dye was used with a suitable optical filter for identifying the interface location and slope, while the latter, used with a UV black light, permitted user observation of the experiment. Nominally, the same concentration of silver particles was used in the oil phase, subject to periodic replenishing due to drop out. The aqueous solution was vacuum degassed *in situ* once loaded into the experiment to remove bubbles.

To perform the PIV measurements, a 532 nm Nd:YAG double-pulsed laser beam was steered along the channel centerline via mirrors to the desired imaging location, the beam [visible in Fig. 1(a)] being admitted through the upper curved channel wall. Imaging was conducted through the flat vertical side walls. A synchronized camera capable of capturing rapid frame pairs (PCO AG, PCO1600, 1600 × 1200 pixels) was used and equipped with a ×10 long working distance microscope objective (infinity corrected and followed by the appropriate image forming lens). *In situ* calibration with a *submerged* TEM grid provided a length scale calibration of 0.889 μm per pixel. The laser beam was steered, and the camera manually slid to each new imaging location before being re-registered with one another; all while flow was running (this complexity restricted the practical number of data points and experimental scope explored). Distances from the apex in this work are the sum total of imaging point to imaging point distances, taking into account slope of the interface. Interframe times varied with imaging location from 115 to 7.0 μs to maintain appropriate interframe pixel shifts. Imaging of the interface then of the flow field was done in stages: several frames of interface imagery, a string of tracer images, followed by several more frames of interface imagery to check for progressive interface drift, with optical filters for fluorescence and laser light together with laser power being interchanged as appropriate. The video included in the supplementary material (Video S1.avi) [99] shows this sequence for an example experimental run, 29 mm upstream of the contraction apex (viscoelastic test system), with the delays for file saving and filter interchange omitted. The video is at 8 Hz (the original imaging speed) and original resolution. Both frames in an image pair are shown, the bottom frame being taken after the top frame and subsequent interframe delay. Contrast has been enhanced in the fluorescence images for illustration purposes. Note that since only one frame was needed for the interface/fluorescence imaging, effort was not made to optimize the intensity of the second laser pulse for that part of the experiment.

Restrictions on the maximum practical seeding density and the presence of out-of-focus image artefacts necessitated image processing and stacking prior to image cross correlation. This was conducted via a program written in LABVIEW: as described in Hodgkinson [34], a pixel was effectively excluded if significant brightness was found in a ring surrounding it, making aberrations and out-of-focus particles disappear (as well as background light). This then permitted stacking of ∼150–160 frame pairs (8 Hz frame pairs or about 20 s of data) taken at each location. Images were also rotated and shifted to make the interface horizontal and vertically centered prior to cross correlation. Cross correlation was performed in PIVview2C (PIVTEC GmbH) to yield vector fields. 32 (H) × 16 (V) pixel interrogation windows were used for this horizontal flow field, with 50% overlap, the grid being refined from an initial size of 64 × 64 pixels. A range of validation conditions were also applied to the vectors obtained. The resulting vector field for an example experimental run 29 mm upstream of the contraction apex is shown in Fig. 1(b), overlaid on a stacked version of the later image of the frame pair (this frame, with a more restrictive illumination spread, dictated the attainable set of vectors). This particular dataset used a 20.36 μs interframe time, giving 43.7 mm s^{-1} per pixel shift.

The stacking of PIV frames being performed necessitated an extremely stable flow field and interface location. This was studied in detail via fluorescence images taken with the Newtonian glycerol-water system. Neglecting viscoelastic instabilities, the higher velocities and very low viscosity of the test phase would have made this system the most susceptible to instability and inadequate pumping oscillation damping. It was found that the worst shift in average interface position between groups of fluorescence images taken before and after taking tracer images was 32 vertical pixels—a measure of progressive interface drift and camera wobble during filter change. The maximum wobble in a group of fluorescence frames was 20 vertical pixels, an indication of flow instability or pulsation and comparable to the height of an interrogation window used (16 pixels). Position instability in a group of fluorescence images was worst at upstream locations. This was reduced close to the contraction apex, the region of most interest, on the account of the relative narrowing of the channel and avoidance of recirculation zones observed in the inlet region. The viscoelastic fluid system was found to be similarly stable, with no sign of any additional forms of instability occurring. This is exemplified by the supplementary material video, the location being intermediate between upstream locations and the channel apex. Additional general videos of the overall flow field are available at the references under the "Data Availability" section.

Using the Newtonian water-glycerol system, velocity profile fitting to these vector fields and the subsequent shear rate measurement procedure was developed. This is detailed in Sec. IV of the supplementary material [99]. This system was then used to validate the experiment before studying the viscoelastic test system. Comments are also made on the flow field symmetry.

For the transient shear history recreation experiments, the DHR2 rheometer was equipped with a cone and plate geometry explicitly loaned for these tests, chosen for minimal internal contributions (anodized aluminum, 0.5°, 60 mm diameter) and programed to recreate the shear rate histories at 22.7 °C. For a hyperbolic channel, shear rate variations are expected to be exponential against time for a Newtonian fluid packet following a streamline. Despite the non-Newtonian system investigated here, this profile works reasonably well with the extensional experiment data. Exponentially fitted shear rates

(i.e., the gray dotted line in Fig. 2, fitted to the gray data points shown) were then integrated to strain and programmed using two exponential functions under the "arbitrary wave" mode in the DHR2 TRIOS instrument software. Suitable motor control settings were established by trial and error, and inertial contributions in the raw data from the geometry and spindle were externally corrected for via a program written in LABVIEW as the they are not removed in this mode of the TRIOS software (v4.1.1.33073). These inertial corrections were checked by performing transient tests on a 0.28 Pa s Newtonian oil and with the geometry rotating in free air, with the correct constant values of viscosity being returned subject to minor oscillation. Inertia corrected data were then fitted as described in the Results section for viscosity oscillation mitigation. In hindsight, as this is a drag-cup motor instrument, programing in terms of stress might have alleviated some of the motor control issues, but at the expense of a potentially worse fit when determining the shear stress profile for rheometer programing.

More details on many aspects of the method, including the design and construction of the experimental setup, can be found in Hodgkinson [34].

REFERENCES

[1] McCrum, N. G., C. P. Buckley, and C. B. Bucknall, *Principles of Polymer Engineering*, 2nd ed (Oxford University, Oxford, 1997).

[2] Cogswell, F. N., "Converging flow of polymer melts in extrusion dies," Polym. Eng. Sci. **12**, 64–73 (1972).

[3] Baird, D. G., "The role of extensional rheology in polymer processing," Korea-Australia Rheol. J. **11**, 305–311 (1999); available at https://www.koreascience.or.kr/article/JAKO199911921263424. page and https://www.cheric.org/research/tech/periodicals/view.php?seq=279834.

[4] Mackley, M. R., "Polymer processing: The physics of stretching chains," Phys. Technol. **9**, 13–19 (1978).

[5] Xu, Z., and C. Gao, "Graphene fiber: A new trend in carbon fibers," Mater. Today **18**, 480–492 (2015).

[6] Xin, G., W. Zhu, Y. Deng, J. Cheng, L. T. Zhang, A. J. Chung, S. De, and J. Lian, "Microfluidics-enabled orientation and microstructure control of macroscopic graphene fibres," Nat. Nanotechnol. **14**, 168–175 (2019).

[7] Tofail, S. A. M., E. P. Koumoulos, A. Bandyopadhyay, S. Bose, L. O'Donoghue, and C. Charitidis, "Additive manufacturing: Scientific and technological challenges, market uptake and opportunities," Mater. Today **21**, 22–37 (2018).

[8] Feilden, E., C. Ferraro, F. Giuliani, L. Vandeperre, and E. Saiz, "Progress in novel and unexpected areas," Mater. Today **19**, 544–545 (2016).

[9] Quan, Z., A. Wu, M. Keefe, X. Qin, J. Yu, J. Suhr, J.-H. Byun, B.-S. Kim, and T.-W. Chou, "Additive manufacturing of multi-directional preforms for composites: Opportunities and challenges," Mater. Today **18**, 503–512 (2015).

[10] Shepherd, G. W., H. G. Clark, and G. W. Pearsall, "Extrusion of polymer tubing using a rotating mandrel," Polym. Eng. Sci. **16**, 827–830 (1976).

[11] Guo, Y., Q. Wang, and S. Bai, "The effect of rotational extrusion on the structure and properties of HDPE pipes," Polym.-Plast. Technol. Eng. **49**, 908–915 (2010).

[12] Li, Y., M. Nie, and Q. Wang, "Facile fabrication of electrically conductive Low-density polyethylene/carbon fiber tubes for novel smart materials via multiaxial orientation," ACS Appl. Mater. Interfaces **10**, 1005–1016 (2018).

[13] Covas, J. A., "Rotating mandrel dies," in *Design of Extrusion Forming Tools*, edited by O. S. Carneiro and J. M. Nóbrega (Smithers Rapra Technology, Shrewsbury, 2012).

[14] Duhduh, A., A. A. Rajhi, and J. P. Coulter, "The impact of the "4d-rheoprinting" additive manufacturing technique on molecular orientation and thermal properties of polymeric parts," TechConnect Briefs **4**, 87–91 (2018); available at https://briefs.techconnect.org/papers/the-impact-of-the-4d-rheoprinting-additive-manufacturing-technique-on-molecular-orientation-and-thermal-properties-of-polymeric-parts/.

[15] Noor, H., K. Alqosaibi, A. Duhduh, A. Kundu, and J. Coulter, "Shear induced crystallization through altering flow area of polymer melt in additive manufacturing," TechConnect Briefs **2019**, 131–134; available at https://briefs.techconnect.org/papers/shear-induced-crystallization-through-altering-flow-area-of-polymer-melt-in-additive-manufacturing/.

[16] Davard, F., and D. Dupuis, "Flow visualisation experiments in a blade coating process," J. Non-Newtonian Fluid Mech. **93**, 17–28 (2000).

[17] Gupta, R. K., R. C. Chan, and A. K. Deysarkar, "Flow of multigrade motor oils in an extensional flow field," J. Rheol. **34**, 1373–1386 (1990).

[18] Bates, T. W., B. Williamson, J. A. Spearot, and C. K. Murphy, "The importance of oil elasticity," Ind. Lubr. Tribol. **40**, 4–19 (1988).

[19] Powell, J., and S. Blackburn, "Co-extrusion of multilayered ceramic micro-tubes for use as solid oxide fuel cells," J. Eur. Ceram. Soc. **30**, 2859–2870 (2010).

[20] Li, T., Z. Wu, and K. Li, "Co-extrusion of electrolyte/anode functional layer/anode triple-layer ceramic hollow fibres for micro-tubular solid oxide fuel cells–electrochemical performance study," J. Power Sources **273**, 999–1005 (2015).

[21] Droushiotis, N., M. H. D. Othman, U. Doraswami, Z. Wu, G. Kelsall, and K. Li, "Novel co-extruded electrolyte–anode hollow fibres for solid oxide fuel cells," Electrochem. Commun. **11**, 1799–1802 (2009).

[22] Li, Y., and H. Pu, "Facile fabrication of multilayer separators for lithium-ion battery via multilayer coextrusion and thermal induced phase separation," J. Power Sources **384**, 408–416 (2018).

[23] Baldwin, R. S., M. Guzik, and M. Skierski, Properties and performance attributes of novel co-extruded polyolefin battery separator materials. Part 1: Mechanical properties, NASA STI Program, NASA/TM—2011-216979/PART1 (NASA, Washington, DC, 2011); available at https://ntrs.nasa.gov/citations/20110008276.

[24] Arvedson, M. A. M, "Rheological considerations in coextrusion," J. Plast. Film Sheeting **1**, 22–29 (1985).

[25] Dooley, J., and L. Rudolph, "Viscous and elastic effects in polymer coextrusion," J. Plast. Film Sheeting **19**, 111–122 (2003).

[26] Huang, W., J. Dooley, K. A. Koppi, D. Bhattacharjee, and R. J. Koopmans, "Effect of rheology on the morphology of coextruded microcapillary films," in *SPE Antec 2015*, Orlando, FL, 23–25 March 2015 (Society of Plastics Engineers, Danbury, CT, 2015); available at https://plasticsengineering.files.wordpress.com/2015/07/p2093628.pdf.

[27] Dooley, J., "Viscoelastic flow effects in multilayer polymer coextrusion", Ph.D. Thesis, TU Eindhoven, Eindhoven, 2002.

[28] Chen, Y., L. J. Struble, and G. H. Paulino, "Using rheology to achieve co-extrusion of cement-based materials with graded cellular structures," Int. J. Appl. Ceram. Technol. **5**, 513–521 (2008).

[29] Powell, J., and S. Blackburn, "The unification of paste rheologies for the co-extrusion of solid oxide fuel cells," J. Eur. Ceram. Soc. **29**, 893–897 (2009).

[30] Beeaff, D. R., and G. E. Hilmas, "Rheological behavior of coextruded multilayer architectures," J. Mater. Sci. **37**, 1259–1264 (2002).

[31] Ismael, M. R., F. Clemens, W. M. Bohac, T. Graule, and M. J. Hoffmann, "Effects of rheology on the interface of Pb(Zr, Ti)O_3

monofilament composites obtained by co-extrusion," J. Eur. Ceram. Soc. **29**, 3015–3021 (2009).
[32] McKinley, G. H., "Thixotropy, mnemosyne and the rheology of remembrance," in 18th International Congress on Rheology, Rio de Janeiro, 14–17 December 2020, 2020.
[33] Bird, R. B., R. C. Armstrong, and O. Hassager, *Dynamics of Polymeric Liquids*, 2nd ed (Wiley, York, 1987), Vol. 1.
[34] Hodgkinson, R., "The effect of extensional flow on shear viscosity," Ph.D. Thesis, The University of Sheffield, Sheffield, 2017; available at https://etheses.whiterose.ac.uk/18327/.
[35] Evans, M. W., and D. M. Heyes, "Combined shear and elongational flow by non-equilibrium molecular dynamics," Mol. Phys. **69**, 241–263 (1990).
[36] Astarita, G., "Quasi-Newtonian constitutive equations exhibiting flow-type sensitivity," J. Rheol. **35**, 687–689 (1991).
[37] Tseng, H.-C., "A revisitation of generalized Newtonian fluids," J. Rheol. **64**, 493–504 (2020).
[38] Bharati, A., S. D. Hudson, and K. M. Weigandt, "Poiseuille and extensional flow small-angle scattering for developing structure–rheology relationships in soft matter systems," Curr. Opin. Colloid Interface Sci. **42**, 137–146 (2019).
[39] Yang, H., D. Liu, J. Ju, J. Li, Z. Wang, G. Yan, Y. Ji, W. Zhang, G. Sun, and L. Li, "Chain deformation on the formation of shish nuclei under extension flow: An *in situ* SANS and SAXS study," Macromolecules **49**, 9080–9088 (2016).
[40] Lopez, C. G., T. Watanabe, A. Martel, L. Porcar, and J. T. Cabral, "Microfluidic-SANS: Flow processing of complex fluids," Sci. Rep. **5**, 7727 (2015).
[41] Penfold, J., E. Staples, I. Tucker, P. Carroll, I. Clayton, J. S. Cowan, G. Lawton, S. Amin, A. Ferrante, and N. Ruddock, "Elongational flow induced ordering in surfactant micelles and mesophases," J. Phys. Chem. B **110**, 1073–1082 (2006).
[42] McCready, E. M., and W. R. Burghardt, "Structural response of a prealigned cylindrical block copolymer melt to extensional flow," J. Rheol. **59**, 935–956 (2015).
[43] Ellison, M. S., P. E. Lopes, and W. T. Pennington, "In-situ x-ray characterization of fiber structure during melt spinning," J. Eng. Fibers Fabr. **3**, 155892500800300 (2008).
[44] Heeley, E. L., T. Gough, D. J. Hughes, W. Bras, J. Rieger, and A. J. Ryan, "Effect of processing parameters on the morphology development during extrusion of polyethylene tape: An in-line small-angle x-ray scattering (SAXS) study," Polymer **54**, 6580–6588 (2013).
[45] López-Barrón, C. R., W. R. Burghardt, and M. S. Kweon, "Local and global stretching of polymer chains during startup of extensional flow," ACS Macro Lett. **9**, 26–31 (2020).
[46] Bent, J., L. R. Hutchings, R. W. Richards, T. Gough, R. Spares, P. D. Coates, I. Grillo, O. G. Harlen, D. J. Read, R. S. Graham, A. E. Likhtman, D. J. Groves, T. M. Nicholson, and T. C. B. McLeish, "Neutron-mapping polymer flow: Scattering, flow visualization, and molecular theory," Science **301**, 1691–1695 (2003).
[47] Lutz-Bueno, V., J. Kohlbrecher, and P. Fischer, "Micellar solutions in contraction slit-flow: Alignment mapped by SANS," J. Non-Newtonian Fluid Mech. **215**, 8–18 (2015).
[48] Qazi, S. J. S., A. R. Rennie, I. Tucker, J. Penfold, and I. Grillo, "Alignment of dispersions of plate-like colloidal particles of $Ni(OH)_2$ induced by elongational flow," J. Phys. Chem. B **115**, 3271–3280 (2011).
[49] Corona, P. T., N. Ruocco, K. M. Weigandt, L. G. Leal, and M. E. Helgeson, "Probing flow-induced nanostructure of complex fluids in arbitrary 2D flows using a fluidic four-roll mill (FFoRM)," Sci. Rep. **8**, 15559 (2018).
[50] Cinader, D. K., and W. R. Burghardt, "X-ray scattering studies of orientation in channel flows of a thermotropic liquid–crystalline polymer," J. Polym. Sci., Part B: Polym. Phys. **37**, 3411–3428 (1999).
[51] Trebbin, M., D. Steinhauser, J. Perlich, A. Buffet, S. V. Roth, W. Zimmermann, J. Thiele, and S. Förster, "Anisotropic particles align perpendicular to the flow direction in narrow microchannels," Proc. Natl. Acad. Sci. U.S.A. **110**, 6706–6711 (2013).
[52] Martin, H. P., N. J. Brooks, J. M. Seddon, P. F. Luckham, N. J. Terrill, A. J. Kowalski, and J. T. Cabral, "Microfluidic processing of concentrated surfactant mixtures: Online SAXS, microscopy and rheology," Soft Matter **12**, 1750–1758 (2016).
[53] Cogswell, F. N., "Converging flow and stretching flow: A compilation," J. Non-Newtonian Fluid Mech. **4**, 23–38 (1978).
[54] Wunderlich, A. M., and D. F. James, "Extensional flow resistance of dilute polyacrylamide and surfactant solutions," Rheol. Acta **26**, 522–531 (1987).
[55] Vissmann, K., and H.-W. Bewersdorff, "The influence of pre-shearing on the elongational behaviour of dilute polymer and surfactant solutions," J. Non-Newtonian Fluid Mech. **34**, 289–317 (1990).
[56] Soulages, J. M., G. H. McKinley, N. R. Hall, K. S. Magee, G. E. Chamitoff, and E. M. Fincke, "Extensional properties of a dilute polymer solution following preshear in microgravity," in *Earth and Space 2010 (12th Biennial International Conference on Engineering, Construction, and Operations in Challenging Environments)*, Honolulu, HI, 14–17 March 2010 (American Society of Civil Engineers, Reston, VA, 2010), pp. 2199–2206.
[57] Jaishankar, A., S. Haward, N. R. Hall, K. S. Magee, and G. H. McKinley, "Shear history extensional rheology experiment II (SHERE II) microgravity rheology with non-Newtonian polymeric fluids," in *2012 American Society for Gravitational and Space Research (ASGSR) Meeting, New Orleans, LA, 28 November–1 December 2012* ([NASA Scientific and Technical Information (STI) Program, Hampton, VA, 2013]; available at https://ntrs.nasa.gov/citations/20130011410.
[58] Yao, M., and G. H. McKinley, "Shear history effects on extensional flow of non-Newtonian fluids in filament stretching rheometers," AIP Conf. Proc. **1027**, 243–245 (2008).
[59] Bhardwaj, A., D. Richter, M. Chellamuthu, and J. P. Rothstein, "The effect of pre-shear on the extensional rheology of wormlike micelle solutions," Rheol. Acta **46**, 861–875 (2007).
[60] James, D. F., B. D. McLean, and J. H. Saringer, "Presheared extensional flow of dilute polymer solutions," J. Rheol. **31**, 453–481 (1987).
[61] Wagner, C. E., and G. H. McKinley, "The importance of flow history in mixed shear and extensional flows," J. Non-Newtonian Fluid Mech. **233**, 133–145 (2016).
[62] Fuller, G. G., and L. G. Leal, "Flow birefringence of concentrated polymer solutions in two-dimensional flows," J. Polym. Sci.: Polym. Phys. Ed. **19**, 557–587 (1981).
[63] Mezi, D., G. Ausias, S. G. Advani, and J. Férec, "Fiber suspension in 2D nonhomogeneous flow: The effects of flow/fiber coupling for Newtonian and power-law suspending fluids," J. Rheol. **63**, 405–418 (2019).
[64] Sommer, D. E., A. J. Favaloro, and R. B. Pipes, "Coupling anisotropic viscosity and fiber orientation in applications to squeeze flow," J. Rheol. **62**, 669–679 (2018).
[65] Lee, K., M. R. Mackley, T. C. B. McLeish, T. M. Nicholson, and O. G. Harlen, "Experimental observation and numerical simulation of transient 'stress fangs' within flowing molten polyethylene," J. Rheol. **45**, 1261–1277 (2001).

[66] Haward, S. J., M. S. N. Oliveira, M. A. Alves, and G. H. McKinley, "Optimized cross-slot flow geometry for microfluidic extensional rheometry," Phys. Rev. Lett. **109**, 128301 (2012).
[67] Varchanis, S., J. Tsamopoulos, A. Q. Shen, and S. J. Haward, "Reduced and increased flow resistance in shear-dominated flows of Oldroyd-B fluids," J. Non-Newtonian Fluid Mech. **300**, 104698 (2022).
[68] James, D. F., G. M. Chandler, and S. J. Armour, "A converging channel rheometer for the measurement of extensional viscosity," J. Non-Newtonian Fluid Mech. **35**, 421–443 (1990).
[69] Guillot, P., P. Panizza, J.-B. Salmon, M. Joanicot, A. Colin, C.-H. Bruneau, and T. Colin, "Viscosimeter on a microfluidic chip," Langmuir **22**, 6438–6445 (2006).
[70] Guillot, P., T. Moulin, R. Kötitz, M. Guirardel, A. Dodge, M. Joanicot, A. Colin, C.-H. Bruneau, and T. Colin, "Towards a continuous microfluidic rheometer," Microfluidics Nanofluidics **5**, 619–630 (2008).
[71] Gachelin, J., G. Miño, H. Berthet, A. Lindner, A. Rousselet, and É. Clément, "Non-Newtonian viscosity of *Escherichia coli* suspensions," Phys. Rev. Lett. **110**, 268103 (2013).
[72] Williams, P. R., and R. W. Williams, "On the planar extensional viscosity of mobile liquids," J. Non-Newtonian Fluid Mech. **19**, 53–80 (1985).
[73] Everage, A. E., and R. L. Ballman, "The extensional flow capillary as a new method for extensional viscosity measurement," Nature **273**, 213–215 (1978).
[74] Winter, H. H., C. W. Macosko, and K. E. Bennett, "Orthogonal stagnation flow, a framework for steady extensional flow experiments," Rheol. Acta **18**, 323–334 (1979).
[75] van Aken, J. A., and H. Janeschitz-Kriegl, "New apparatus for the simultaneous measurement of stresses and flow birefringence in biaxial extension of polymer melts," Rheol. Acta **19**, 744–752 (1980).
[76] Macosko, C. W., M. A. Ocansey, and H. H. Winter, "Steady planer extension with lubricated dies," J. Non-Newtonian Fluid Mech. **11**, 301–316 (1982).
[77] Wang, J., and D. F. James, "Lubricated extensional flow of viscoelastic fluids in a convergent microchannel," J. Rheol. **55**, 1103–1126 (2011).
[78] Kim, H. C., A. Pendse, and J. R. Collier, "Polymer melt lubricated elongational flow," J. Rheol. **38**, 831–845 (1994).
[79] Sousa, P. C., F. T. Pinho, M. S. N. Oliveira, and M. A. Alves, "Extensional flow of blood analog solutions in microfluidic devices," Biomicrofluidics **5**, 014108 (2011).
[80] Haward, S. J., A. Jaishankar, M. S. N. Oliveira, M. A. Alves, and G. H. McKinley, "Extensional flow of hyaluronic acid solutions in an optimized microfluidic cross-slot device," Biomicrofluidics **7**, 044108 (2013).
[81] Calabrese, V., S. J. Haward, and A. Q. Shen, "Effects of shearing and extensional flows on the alignment of colloidal rods," Macromolecules **54**, 4176–4185 (2021).
[82] Haward, S. J., T. J. Ober, M. S. N. Oliveira, M. A. Alves, and G. H. McKinley, "Extensional rheology and elastic instabilities of a wormlike micellar solution in a microfluidic cross-slot device," Soft Matter **8**, 536–555 (2012).
[83] Sousa, P. C., F. T. Pinho, and M. A. Alves, "Purely-elastic flow instabilities and elastic turbulence in microfluidic cross-slot devices," Soft Matter **14**, 1344–1354 (2018).
[84] Oliveira, M. S. N., M. A. Alves, F. T. Pinho, and G. H. McKinley, "Viscous flow through microfabricated hyperbolic contractions," Exp. Fluids **43**, 437–451 (2007).
[85] Oliveira, M. S. N., L. E. Rodd, G. H. McKinley, and M. A. Alves, "Simulations of extensional flow in microrheometric devices," Microfluid. Nanofluid. **5**, 809–826 (2008).
[86] Wereley, S. T., and C. D. Meinhart, "Recent advances in micro-particle image velocimetry," Annu. Rev. Fluid Mech. **42**, 557–576 (2010).
[87] Wiklund, J., I. Shahram, and M. Stading, "Methodology for in-line rheology by ultrasound Doppler velocity profiling and pressure difference techniques," Chem. Eng. Sci. **62**, 4277–4293 (2007).
[88] Rowe, W. B., *Hydrostatic, Aerostatic, and Hybrid Bearing Design* (Elsevier, Amsterdam, 2012), p. 29.
[89] Park, J. M., "Comment on 'A revisitation of generalized Newtonian fluids' [J. Rheol. **64**, 493–504 (2020)]," J. Rheol. **64**, 1497–1499 (2020).
[90] Whorlow, R. W., *Rheological Techniques*, 2nd ed. (Ellis Horwood, New York, 1992).
[91] Doshi, S. R., and J. M. Dealy, "Exponential shear: A strong flow," J. Rheol. **31**, 563–582 (1987).
[92] Kang, K., L. J. Lee, and K. W. Koelling, "High shear microfluidics and its application in rheological measurement," Exp. Fluids **38**, 222–232 (2005).
[93] Petrie, C. J. S., "Extensional viscosity: A critical discussion," J. Non-Newtonian Fluid Mech. **137**, 15–23 (2006).
[94] Giesekus, H., "A simple constitutive equation for polymer fluids based on the concept of deformation-dependent tensorial mobility," J. Non-Newtonian Fluid Mech. **11**, 69–109 (1982).
[95] Torres, M. D., B. Hallmark, D. I. Wilson, and L. Hilliou, "Natural Giesekus fluids: Shear and extensional behavior of food gum solutions in the semidilute regime," AIChE J. **60**, 3902–3915 (2014).
[96] Gauri, V., and K. W. Koelling, "Extensional rheology of concentrated poly(ethylene oxide) solutions," Rheol. Acta **36**, 555–567 (1997).
[97] Dai, S., and K. C. Tam, "Effect of cosolvents on the binding interaction between poly(ethylene oxide) and sodium dodecyl sulfate," J. Phys. Chem. B **110**, 20794–20800 (2006).
[98] Hodgkinson, R., "The effect of extensional flow on shear viscosity," The University of Sheffield ORDA (Online Research Data Repository), 2017.
[99] See supplementary material at https://www.scitation.org/doi/suppl/10.1122/8.0000380 for a PDF document outlining several additional considerations as directly referenced throughout this text. An example video of raw experimental imagery is also included (Video S1.avi) as referred to briefly in the detailed methods in the Appendix.